Fracture Toughness of Free-Standing $ZrSi_x$ Thin Films Measured Using Crack-on-a-Chip Method

Airat Shafikov, Robbert van de Kruijs, Jos Benschop, Wesley van den Beld, Silvester Houweling, and Fred Bijkerk

***Abstract*— In this work, we experimentally measure fracture toughness of free-standing zirconium $ZrSi_x$ thin films using the crack-on-a-chip method. In this method, fracture toughness is determined from the analysis of cracks, which propagate and arrest in specially designed free-standing test structures. The test structures use a well-known double cantilever beam geometry, which enables crack arrest, and don't require any external force actuation, but instead rely on the internal tensile stress of the tested thin film. To produce the $ZrSi_x$ test structures, a universal fabrication process was developed and used, which avoids typical issues related to etch selectivity and that can be readily applied for other thin film materials. Unlike in previous studies, which used the crack-on-a-chip method, in this work crack initiation was triggered only after the test structures were fully fabricated, which allowed to avoid the influence of the fabrication process on the extracted toughness values. For this, blunt pre-cracks included in the structures were "sharpened" using focused ion beam, which resulted in rapid crack propagation and subsequent crack arrest. Mechanical analysis done by a finite element method to extract the values of fracture toughness, showed that buckling of the free-standing thin film test structures has a strong influence on the results of fracture toughness calculations and therefore cannot be ignored. The fracture toughness of $ZrSi_x$ thin films was determined to be 2.1±0.13 $MPa*m^{0.5}$.**

[2021-0166]

***Index Terms*— Fracture toughness, thin films, free-standing, buckling, method, EUV pellicle.**

I. Introduction

ADVANCES in thin film technology and microfabrication have been made continuously over the past decades, which now allows for fabrication and use of free-standing thin films in various applications, such as MEMS-based sensors, actuators, and electron and x-ray transparent membranes. A particularly challenging application is the use of large-scale free-standing ultra-thin films in extreme ultraviolet (EUV) pellicles. The large free-standing area (10 cm × 14 cm), high internal tensile stresses (several hundreds of MPa or higher), and extremely small thickness (sub 50 nm) make EUV pellicles susceptible to mechanical failure. The reliability of an EUV pellicle is often limited not by the intrinsic tensile strength of the material, but by fabrication-induced defects. In the presence of a defect, the maximum stress that the material can withstand without fracture, i.e. the fracture strength σ_f, is determined by the fracture toughness parameters K_{IC}, K_{IIC}, and K_{IIIC}, corresponding to three fracture modes, respectively: mode I (crack opening mode: tensile stress perpendicular to the crack surface), mode II (sliding mode: shear stress parallel to the crack surface and perpendicular to the crack front), and mode III (tearing mode: shear stress parallel to the crack surface and the crack front). In free-standing membranes with uniform equi-biaxial internal stress, such as EUV pellicles, fracture predominantly happens via mode I [1], [2] and fracture strength can be determined as $\sigma_f = \frac{K_{IC}}{\sqrt{2\pi a}}$, where a is the size of the flaw (e.g. crack). Characterization and improvement of fracture toughness are essential for designing mechanically strong and reliable free-standing thin film components, including EUV pellicles. Despite this, however, the literature shows no reports on the characterization of the fracture toughness of metal silicide thin films, which are considered to be promising candidate materials for the next generation EUV pellicles thanks to their high thermal stability, yield strength, and EUV transmission [3].

The common approach for determining fracture toughness is to introduce a defect in the tested material, i.e., a pre-crack, and measure the mechanical load required to initiate fracture. For a free-standing thin film, manufacturing a pre-crack and the application of a load become increasingly more challenging as the thickness of the tested film decreases. Several different techniques have been developed to address these challenges. For instance, some researchers used a method, in which fracture toughness is determined by measuring the load needed to initiate fracture from blunt pre-cracks produced by lithography or Focused Ion Beam (FIB) [4], [5]. However, while relatively easy to manufacture, blunt pre-cracks lead to over-estimation of fracture toughness values determined

Manuscript received August 5, 2021; revised October 21, 2021; accepted November 1, 2021. This work is part of the research programme of the Industrial Focus Group XUV Optics, being part of the MESA+ Institute for Nanotechnology and the University of Twente, (www.utwente.nl/xuv) and the Industrial Partnership Programme "X-tools" (project No. 741.018.301), the latter being financed by the Dutch Research Council (NWO), ASML, Carl Zeiss SMT, Malvern Panalytical and the MESA+ Institute for Nanotechnology. Subject Editor D. Elata. *(Corresponding author: Airat Shafikov.)*

Airat Shafikov, Robbert van de Kruijs, Wesley van den Beld, and Fred Bijkerk are with the Industrial Focus Group XUV Optics, MESA + Institute of Nanotechnology, University of Twente, 7522 NB Enschede, The Netherlands (e-mail: a.shafikov@utwente.nl).

Jos Benschop and Silvester Houweling are with the Industrial Focus Group XUV Optics, MESA + Institute of Nanotechnology, University of Twente, 7522 NB Enschede, The Netherlands, and also with ASML Netherlands B.V., 5504 DR Veldhoven, The Netherlands.

Color versions of one or more figures in this article are available at https://doi.org/10.1109/JMEMS.2021.3128760.

Digital Object Identifier 10.1109/JMEMS.2021.3128760

from the onset of fracture, especially for brittle materials. In order to be representative of a real crack, the radius of curvature of the pre-crack needs to be smaller than the size of the process zone, which in brittle materials can be as low as several nanometers, much smaller than what is available using lithography or FIB. To avoid this over-estimation of the fracture toughness, several researchers used pre-cracks introduced by nanoindentation [6], [7], [8], [9]. For this, the area on the substrate is indented next to the patterned thin film before it is released from the substrate, which results in an atomically sharp arrested crack in the thin film. Still, applying mechanical load to the tested film remains challenging, as it requires the use of special actuator devices fabricated on-chip [6], [7] or external actuation [9], which must be carefully aligned with the sample. Another novel method of thin film toughness characterization that does not require any external actuation or introduction of atomically sharp pre-cracks was recently proposed by Jaddi *et al.* [10], [12]. The method uses specially designed internally stressed test structures to initiate and arrest atomically sharp cracks in free-standing thin film samples. In this method, the tested film is patterned to form special test structures, which upon release from the substrate produce atomically sharp arrested cracks, that are afterwards analysed to extract the fracture toughness. Crack propagation is enabled by the pulling force, which can be created by the internal tensile stress in the tested thin film [10] or, if the tested film is compressive, by a second dedicated thin film layer with known tensile stress [12]. The method has two big advantages, which make it very attractive for studying fracture in free-standing thin films. First, fracture toughness is extracted from the analysis of atomically sharp cracks, which avoids over-estimation that is inherent to the methods that use crack initiation from a blunt pre-crack. Second, cracks are initiated and propagated by the internal stresses, which significantly simplifies and speeds up the testing procedure compared to the other methods, which require very careful application of external forces.

While the crack-on-a-chip method has clear advantages over other toughness measurement techniques, several challenges remain, such as avoiding the influence of the fabrication process on crack propagation, which occurs while the test structures are being released from the substrate, and the need to improve the mechanical analysis by taking into account the out of plane deformations of the free-standing thin film test structures. The goal of this work is to address the shortcomings of the original crack-on-a-chip test method and apply it to measure mode I fracture toughness of $ZrSi_x$ thin films, one of the candidate materials for EUV pellicle cores.

II. Crack-on-a-Chip Test

In the crack-on-a-chip method, a free-standing thin film is patterned to form a double cantilever beam (DCB) [11] test structure. A schematic of the test structure configuration used in this work is given in Fig. 1. The structure consists of a sample beam containing a pre-crack and two actuator beams, which apply pulling force on the sample as a result of the internal tensile stress in the film. If the force provided by the

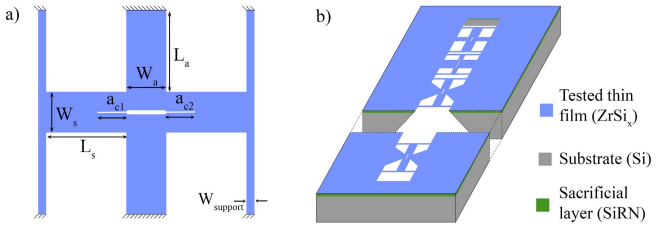

Fig. 1. (a) Top-view schematics of a test structure used in the crack-on-a-chip test method in this work. (b) Bird's eye view 3D schematic showing multiple free-standing test structures with varied designs produced on a single chip.

actuator beams is sufficient, a crack will initiate from the tip of the pre-crack and propagate along the sample beam. Instead of being directly clamped to a the rigid substrate, both ends of the sample are attached to the narrow support beams, which act similarly to the spring-type supports used in [12]. The use of flexible supports allows for some amount of deformation and relaxation of stress acting along the sample beam in the direction of crack propagation. This helps to improve the directional stability of cracks and minimize crack kinking issues frequently observed in test structures with the original configuration, in which the sample was directly clamped to the substrate [10]. Thanks to the DCB geometry, the static energy release rate G_s driving the crack propagation, which is given by $G_s(a) = -\frac{1}{t}\frac{\partial U(a)}{\partial a}$ (where U is the elastic energy stored in the test structure and t is the film thickness), decreases with the increase of crack length a. As a result, the crack will arrest after reaching a certain length a_c. By knowing the length of the arrested crack, the dimensions, and elastic properties of the test structure, one can perform mechanical analysis to determine fracture energy G_c (energy spent on crack creation) and fracture toughness K_{IC} (not to be confused with the generic term *toughness*, which is commonly used to refer to both fracture toughness K_{IC} and fracture energy G_c):

$$K_{IC} = \sqrt{G_c E} \tag{1}$$

where E is Young's modulus.

To extract fracture toughness, one needs to consider the history of the fracture process. In the original experiment scheme used by Jaddi *et al.* [10], [12] crack propagation happens in two stages: rapid crack propagation and slow stable crack propagation. To make the slow stable fracture stage possible without the use of controlled actuation, the dimensions of the test structure pattern are selected such, that the sample beam is released from the substrate first, while the released (free-standing) length of the actuators L_a pulling on the sample beam is gradually increases during the etch process. As a result, value of static energy release rate G_s, which drives the crack, continuously increases during the release process. Once the load provided by the actuators is sufficient, a crack initiates from the tip of the pre-crack and starts rapid propagation [13]. At the beginning of the rapid propagation stage, the energy release rate $G_s(a, L_a)$ is higher than the fracture energy G_c dissipated by the crack. As a result, the excess released elastic energy is temporarily stored in form of kinetic energy and pressure waves. As the crack length

a increases, the energy release rate $G_s(a, L_a)$ decreases and eventually becomes lower than G_c. After this moment, the energy deficit required for further propagation is covered by the stored kinetic energy. Eventually, when all kinetic energy is depleted and the value of $G_s(a, L_a)$ is not sufficient to sustain further propagation, the crack arrests. The final crack length, a, formed after the first propagation stage is determined by the energy balance:

$$G_c = \int_0^a \frac{G_s\,(x, L_a)\,dx}{a} = \frac{1}{\mathrm{t}} \frac{U\,(0, L_a) - U(a, L_a)}{a} \quad (2)$$

where $U\,(0, L_a)$ and $U\,(a, L_a)$ are the values of elastic strain energy stored in the free-standing test structure just before crack initiation (zero crack length) and after crack arrest, respectively and t is the thickness of the test structure (thin film). Note that actuators are released slowly and their free-standing length L_a is virtually unchanged during the rapid crack propagation stage. The etch process is then continued, which leads to a further increase of the length of the free-standing part of the actuator beams L_a and, as a result, increase of $G_s(a, L_a)$. Once the value of $G_s(a, L_a)$ reaches the value of fracture energy G_c, the crack continues propagation in the slow stable regime and arrests only when the release process is complete (i.e. when the actuators have been made fully free-standing). During the slow crack propagation stage, the static energy release rate is constant and equal to the fracture energy:

$$G_c = G_s\,(a, L_a) = -\frac{1}{t} \frac{\partial U\,(a, L_a)}{\partial a} \quad (3)$$

By analysing the cracks in the final released structures and using equation 3, one can then determine the fracture energy G_c and corresponding fracture toughness K_{IC} of the studied thin film material. However, this approach, in which crack initiation and propagation occurs during sample fabrication has some shortcomings. First, the excess energy released at the beginning of the rapid propagation stage can cause an "overshoot" of the crack length, leading to the situation when the energy release rate is too low to enable further slow crack propagation even when actuators are fully released. Therefore, to avoid the risk of under-estimation of the G_c values, it is necessary to ensure that the rapid propagation stage is indeed followed by a slow one, for example by periodically stopping the release process and measuring crack length. The second shortcoming is that crack propagation occurs during the etching of the substrate in a chemically active environment. This can influence the results of the measurements in case the tested layer is not perfectly resistant to the etchant or if the etchant species adsorb on the crack surfaces changing the surface energy [14], [15]. Furthermore, when a liquid etchant is used to release the test structure, supercritical drying must be used to prevent liquid surface tension forces from affecting the arrested crack.

In order to avoid these issues, in this work, the experimental procedure was modified such, that crack propagation happened only after sample fabrication was complete. For this, tests structures were produced, which didn't produce enough force to initiate the crack from the blunt pre-crack. The pre-cracks in the un-cracked free-standing test structures were then sharpened using Ga focused ion beam (FIB) milling, which increased the stress concentration at the tip of the pre-crack causing crack initiation. As a result, crack propagation and arrest occurred in the vacuum of the FIB chamber, preventing any environmental impact on the measured fracture toughness. It is important to note, that in this case, crack propagation occurs in a single rapid stage. Therefore, the value of fracture energy G_c is determined from the total amount of elastic energy released during crack propagation (equation 2), rather than from the value of static energy release G_s (equation 3), like in the original crack-on-a-chip method, where the fracture ends with slow crack propagation.

III. Modelling

A. 3D FEM Simulations of Buckled Crack-on-a-Chip Test Structures

In this section, we describe the details of 3D finite element method (FEM) simulations, which were used to calculate G_c values in the experiment. In comparison with the previous studies [10], [12], which use 2D plane stress approximation, analysis done in this work takes into account the out-of-plane buckling of the thin film test structures, which, as will be shown in section III B, has a significant influence on the extracted G_c and, as a result, K_{Ic} values.

In this work, fracture energy analysis was done by evaluating elastic strain energy with static FEM simulations. For this, for each propagated and arrested crack analysed in the experiment (section V A), two static FEM simulations were performed: one replicating the un-cracked structure and another one replicating the structure with the arrested crack. Fracture energy was then determined as the difference in the elastic energy stored in the static test structure before and after fracture (which was evaluated using the built-in function in the simulation software) divided by the fracture area, i.e. using equation 2 (the exact expressions are given further in section V A, along with the details of the experimental procedure).

Static 3D FEM simulations and evaluation of the elastic energy stored in thin film structures were done using Structural Mechanics module in Comsol Multiphysics software package [16]. The material was described using a linear elastic isotropic model and the initial condition was set to be a uniform equi-biaxial plane stress state, mimicking the stress state in the thin film before patterning and release. A fixed boundary condition was applied at the ends of the support beams and the actuator beams, which in the real structures are connected to the rigid substrate, whereas the rest of the structure was allowed to relax.

When the initial stresses are acting in-plane and no external forces in the out-of-plane direction are applied, the 3D model produces a flat solution with no out-of-plane displacements, equivalent to a solution that can be obtained using 2D plane stress approximation. Fig. 2a-b show the distribution of the stresses acting along the x and y-axis in the case of such a flat solution, which was obtained for a typical test structure. As can be seen in Fig. 2a, even though initial stress in the

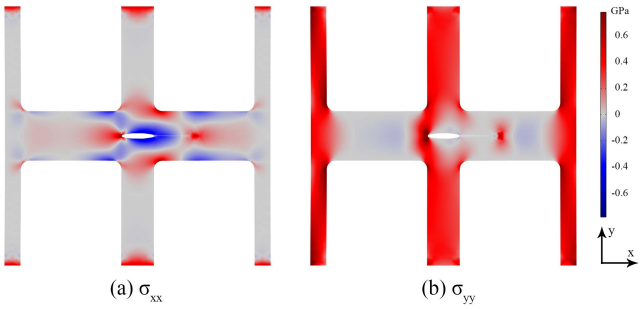

Fig. 2. Distribution of (a) σ_{xx} and (b) σ_{yy} stress in the flat test structure, i.e. with no out-of-plane displacements. Simulation parameters: $E = 180$ GPa, $t = 90$ nm, $\upsilon = 0.2$, $\sigma_0 = 470$ MPa, $W_a = 20$ um, $W_s = 30$ um, $L_s = 60$ um, $L_a = 60$ um, $W_{support} = 10$ um, $a_{c1} = 0$ um (no crack on the left side), $a_{c2} = 34$ um (right crack).

film is tensile, the stationary stress distribution formed upon relaxation of the model is characterized by several areas where the σ_{xx} stress is compressive (negative). More specifically, large negative σ_{xx} is developed along each of the 6 free edges of the test structure oriented along the x-axis: two on each side of the crack and four more along each of the edges of the sample beam. These compressively stressed areas are caused by the combination of two factors. First is the relaxation of the stress along the sample beam, which is made possible by the use of deformable support beams, which are introduced to minimize crack kinking issues, discussed in section 2. Second is the Poisson effect [17], which results in the further decrease of σ_{xx} due to relaxation of σ_{yy} near the free edges. In comparison, σ_{yy}, shown in Fig. 2b, remains tensile near the free edges oriented along the y-axis, due to the fixed boundary condition (i.e. attachment to the rigid substrate), which prevents relaxation of stress along the y-axis. As mentioned earlier, such a flat state with large areas of compressive stress is only possible in the idealized model, in which no out-of-plane forces exist. In reality, however, any smallest disturbance can result in the formation of buckles and relaxation of the compressive stress in these areas, which in turn will affect the stress distribution in the rest of the structure. Therefore, buckling needs to be taken into account to allow for accurate fracture toughness determination. The effect of buckling on the values of static energy release rate and elastic energy are discussed in section III B.

To induce buckling in the simulations, external out-of-plane forces were selectively applied to the test structure, specifically to the small (usually about 1 μm^2) areas within each of the 6 regions with high compressive values of σ_{xx}. The direction of force (positive or negative z-direction) applied to each of the regions can be chosen independently, which allows to obtain various physically possible stable buckling modes characterized by the buckling direction in each of the compressive regions. To ensure that the external load does not produce any mechanical work on the test structure and doesn't affect the final stress distribution, the forces were set to be active only if the deflection at the loading point was small (in comparison with the final deflection). Therefore, the external loads automatically "switched-off" after the first several iterations of computation, once the model was forced out of the flat state and began converging to the desired buckling mode. As a result, the values of elastic energy extracted for the final simulated thin film structure were determined only by the geometry (structure and crack dimensions), elastic properties of the thin film (Young's modulus E, Poisson ratio υ and internal stress σ_0), and the particular buckling mode.

It should be noted, that symmetric structures with support beams (used in this work and in [12], also can be referred to as double-DCB) are not the only type of crack-on-a-chip structures, which buckle. Another type is the asymmetric structures (used in [10] and [12], single-DCB), in which one of the sample beam ends is free-hanging and stress relaxation along the sample and, as a result, buckling can occur without the need for use of support beams instead of direct clamping to substrate. It also should be mentioned, that in contrast to symmetric structures with support beams and asymmetric ones, symmetric structures, which are directly clamped to rigid substrate [10], cannot relax tensile stresses acting along the sample beam and, as a result, do not buckle. However, as previously discussed in section 2 and in [10], [12], tensile stress acting along the sample beam makes crack propagation directionally unstable and therefore is unwanted in the crack-on-a-chip test.

B. Influence of Buckling on the Elastic Energy and Static the Energy Release Rate

As discussed in the previous section, presence of buckles influences the stress distribution in the thin film structures, which in turn determines the values of elastic strain energy that are used to calculate fracture energy. Therefore, it is also useful to discuss the influence of buckling on the elastic energy $U(a)$ and the static energy release rate $G_s(a)$ (which is not used for determination of G_c in this work, but is relevant in the case of slow stable crack propagation [10], [12]).

Results of the analysis presented in this section were obtained by performing static FEM simulations of a typical crack-on-a-chip structure containing a single crack. Series of static simulations with systematically varied crack length $a_n = n * \Delta a$ were performed. Elastic energy stored in the simulated structures was evaluated as a function of crack length, and then differentiated using backward finite difference approximation to determine the static energy release rate:

$$G_s(a_n) = \frac{1}{t}\frac{U(a_{n-1}) - U(a_n)}{\Delta a} \tag{4}$$

As noted in the previous section, the buckling mode can be selected in the model by changing the direction of the external forces, which allows to obtain any of the stable modes and, most importantly, match the experimentally observed profile in order to accurately determine U and G_s values. Here, however, to illustrate the effect of buckling, we will only consider a few of the buckling modes together with a flat solution, which was obtained without the application of external forces. The distributions of out-of-plane displacements for the considered buckling modes are presented in Fig. 3. It can be seen, that in each mode there exist 6 separate areas characterized by large displacement (buckles) and those areas correspond to

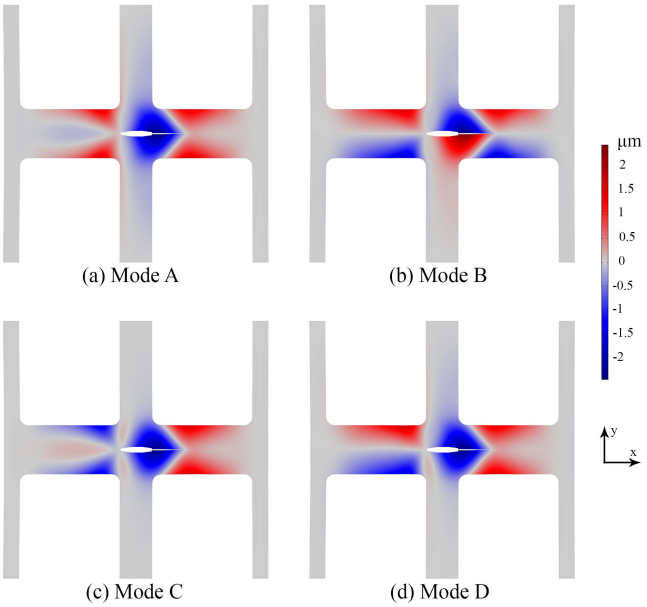

Fig. 3. Distributions of out-of-plane displacement h, which show different examples of stable buckling modes: (a) buckling mode symmetric with respect to x and y axes (mode A), (b) mode antisymmetric w.r.t. x-axis (mode B), (c) example of a mode, symmetric w.r.t x-axis and no symmetricity w.r.t. y-axis (mode C), (d) example of an asymmetric buckling mode (mode D). The simulation parameters are the same as the ones used in *Fig.* 2, with the exception of artificial forces applied to induce buckling.

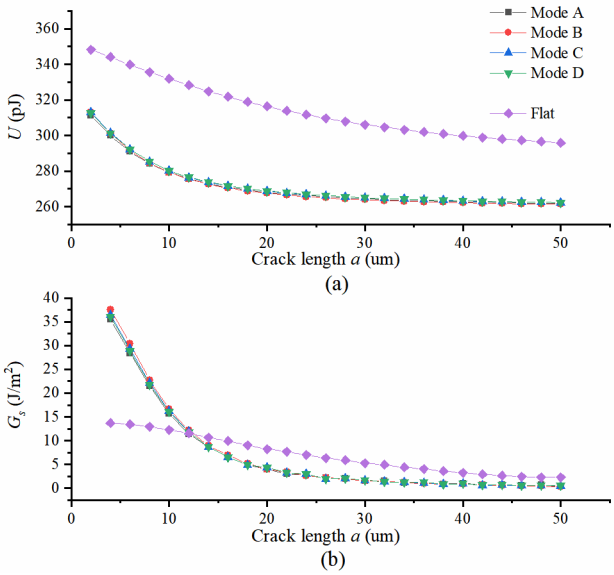

Fig. 4. (a) Total elastic energy U and (b) static elastic energy release G_s for the four buckling modes shown in *Fig.* 3 and a flat solution, with no out-of-plane displacements. The simulation parameters used are the same as the ones used in *Fig.* 2 and *Fig.* 3.

the regions with compressive stress, observed in Fig. 2a. The difference in the direction of each of the 6 main buckles results in slight differences in stress distribution between the buckling modes, which in turn determines the values of elastic energy $U(a)$ and energy release rate $G_s(a)$. Fig. 4 shows the change $U(a)$ and $G_s(a)$, calculated as a derivative of $U(a)$, as a function of the crack length for the modes presented in Fig. 3 and a flat solution. The amount of elastic energy stored in the structure $U(a)$, shown in Fig. 4a, reduces, as crack length increases. The energy release rate $G_s(a)$ driving the crack propagation also decreases as the crack grows, which eventually will cause the crack to arrest. It can be noted, that while both $U(a)$ and $G_s(a)$ differ only slightly between the buckling modes, the difference between the values calculated for the flat solution and any of the buckling modes is much larger. As can be seen from Fig. 4a, relaxation of the compressive stresses by buckling results in a significantly lower amount of energy stored in the buckled structures, compared with the flat one. As a consequence, the values of the energy release rate $G_s(a)$, which is a derivative of $U(a)$, are changed dramatically by taking the buckling into account. As shown in Fig. 4b, with buckles, $G_s(a)$ is about twice higher than in the flat structure when the crack is short, however, for longer cracks the opposite is true. This illustrates the fact that 2D analysis can lead to both under- and over-estimation of the real fracture energy values and therefore shows the importance of taking the out-of-plane displacements into account.

The difference between various buckling modes is much smaller in comparison with the difference between the flat case and any of the buckling modes. The difference in $G_s(a)$ between the modes typically does not exceed 10% and depends on the exact dimensions of the test structure and length of the cracks. Instead, the more important difference between the buckling modes is in the mode of crack loading, or fracture mode. In case when displacements are symmetric along the crack propagation direction, such as the case for modes A and C presented in Fig. 3, the crack is loaded in a pure mode I, i.e. no in-plane or out-of-plane shear stresses act on the crack surface. For the anti-symmetric buckling modes, such as mode B in Fig. 3b, the loading becomes mixed, with an added mode III component, which is characterized by the out-of-plane shear stresses. Finally, when buckling is asymmetric with respect to the direction of crack propagation, the crack loading mode will in general also be mixed and have contributions from all the three modes: in-plane crack opening (mode I), in-plane shear (mode II), and out-of-plane shear (mode III). This, in principle, allows one to study the effect of the loading mode on fracture toughness. However, in the case of the rapid fracture, evaluation of the contribution of the different modes requires a significant modelling effort, due to the need to take into account the movement of the buckled test structure, which can lead to dynamic change of the loading mode during crack propagation. Therefore, the case of symmetric buckling mode (e.g. Fig. 3a and Fig. 3c) is the preferred one for the fracture toughness testing, since it allows for pure mode I type of crack propagation and allows to extract K_{IC}, commonly used to describe fracture resistance of materials.

C. Relation Between the Elastic Properties and the Magnitude of Buckles

Buckling deformation of the thin film structure is determined by its' geometry and elastic properties, namely Young's modulus E, Poisson ratio υ and internal stress σ_0. Since

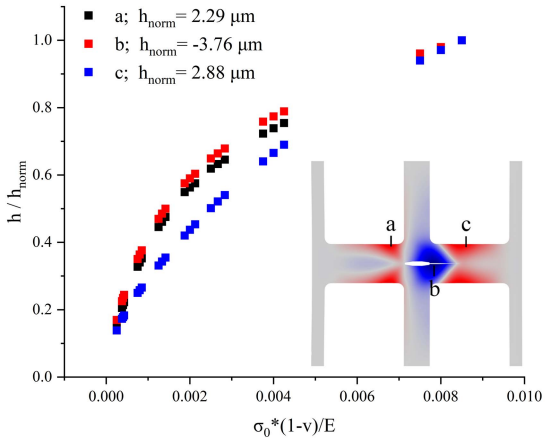

Fig. 5. Normalized out-of-plane displacement h/h_{norm} of the modelled test structure evaluated at different locations on the structure plotted against the ratio between internal stress σ_0 and biaxial modulus $\frac{E}{1-\upsilon}$. The insert indicates locations where displacements were evaluated. Geometric dimension parameters used in simulations are the same as ones given in Fig. 2. Values of σ_0, E and υ in the simulations were varied from 100 to 1000 MPa, from 100 to 300 GPa and from 0.15 to 0.25, respectively.

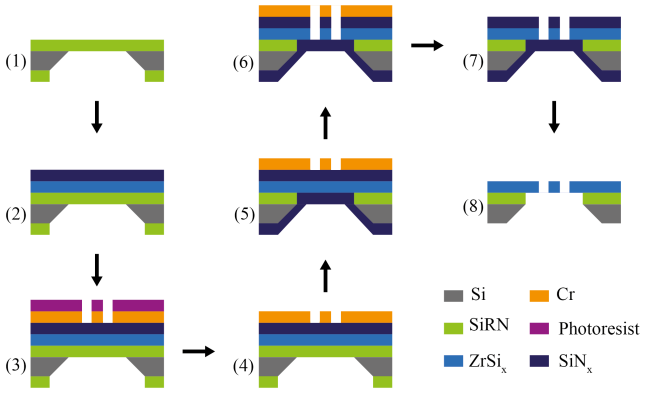

Fig. 6. Schematic of the sample fabrication process.

buckling occurs in discrete buckling modes, the exact mode observed in the experiment can be replicated in FEM simulation and the measured amplitude of the buckles can be thus used to evaluate the elastic properties of the thin film. To establish the relation between the elastic properties of the thin film structure and the magnitude of buckles, we performed a series of simulations with systematically varied values of E, υ and σ_0.

Figure 5 presents the results obtained by FEM for a symmetric buckling mode in a typical crack-on-a-chip structure (FE model was identical to one used to produce Fig. 3a, with the exception that E, υ and σ_0 were varied). The graph shows the values of normalized out-of-plane displacements h/h_{norm} evaluated at several locations in the structure plotted against the ratio between the internal stress σ_0 and the biaxial modulus $\frac{E}{1-\upsilon}$. The values of normalization parameters h_{norm} for each of the considered points (points a, b, c indicated in the insert in Fig.3) correspond to the values of h obtained in the simulation with the largest value of $\frac{\sigma_0(1-\upsilon)}{E}$. As can be seen, for the considered range of parameters (which was chosen to cover the parameters of the studied $ZrSi_x$ films) the buckling profile (i.e. displacement at each point in the structure) is uniquely determined by this ratio, which is also equal to the in-plane strain: $\varepsilon_0 = \frac{\sigma_0(1-\upsilon)}{E}$. In cases, when two out three parameters (E, υ and σ_0) are known or can be measured by a supplementary method, this one-to-one relation between the magnitude of formed buckles and the $\frac{\sigma_0(1-\upsilon)}{E}$ ratio can be used to evaluate the third elastic parameter. As further described in section V, this approach was by us to determine the values of internal stress σ_0 in the $ZrSi_x$ thin film.

IV. Sample Fabrication

To fabricate the $ZrSi_x$ crack-on-a-chip test structures, the process shown in Fig. 6 was used. The main idea behind the developed fabrication process is that during all the steps the $ZrSi_x$ layer is protected by the silicon nitride layers, which are removed by physical sputtering using an Ar ion beam at the last release step. This allows to avoid the selectivity issues, which are often encountered when chemical etching is used and makes the process universal allowing it to be applied for any desired tested layer.

The process starts by preparing free-standing silicon-rich silicon nitride (SiRN) membranes, which are used as substrates for deposition of the tested $ZrSi_x$ layer. The choice of SiRN layer was made because of its low internal stress (using bulge test method [4], [5], [18], SiRN membranes were measured to have internal stress of $\sigma_0 = 0.25$ GPa), which helps to minimize failure of membranes during fabrication. To fabricate SiRN membranes, a 100 nm thick LPCVD SiRN layer is deposited on the front and back sides of 385 μm thick (001) oriented 4 inch Si wafers. The SiRN layer on the backside was patterned using positive resist photolithography and reactive ion etching to form window openings. Following that, Si was etched in 25% tetramethylammonium hydroxide (TMAH) solution at 90° C for approximately 10 hours to form free-standing SiRN thin film membranes (step 1 in Fig. 6). The final thickness of the membrane layer was 83 nm, reduced from the initial value of 100 nm due to the slow etching of the SiRN layer in the TMAH solution.

Free-standing SiRN membranes were then used as substrates for the deposition of the $ZrSi_x$ layer. A 90 nm thick $ZrSi_x$ layer was deposited by magnetron co-sputtering from Si and Zr targets using Ar sputter gas. The composition of the film was close to stoichiometric $ZrSi_2$ and was determined to be $Zr_{0.28}Si_{0.72}$ by Rutherford backscattering spectrometry (RBS). It should be mentioned, that attempts to use exact $ZrSi_2$ stoichiometry were made, however, high tensile stress forming in the stoichiometric $ZrSi_2$ upon crystallization resulted in frequent fracture of the test structures during fabrication. Therefore the focus was made on slightly silicon-rich films ($Zr_{0.28}Si_{0.72}$), which had lower stress and, as a result, much higher yield. To protect the silicide layer during the following processing steps (high-temperature annealing and Cr etch), a thin 5 nm SiN_x layer was deposited as a cap by magnetron sputtering of Si in an $Ar+N_2$ gas mixture. After the $ZrSi_x$ layer was capped, it was annealed for 2 hours at 500° C in

an atmospheric N_2 oven to make the layer thermally stable, induce crystallization and create tensile internal stress.

Patterning was done by using an Ar beam etch. In order to avoid the issues with photoresist mask hardening caused by Ar bombardment [19], patterning of $ZrSi_x$ was done through an intermediate Cr mask. For this, a 300 nm thick Cr layer was deposited by magnetron sputtering and patterned using photolithography and ammonium cerium (IV) nitrate-based wet etchant (step 3). The photoresist layer was then stripped in acetone, followed by rinsing in isopropyl alcohol (step 4). After the Cr mask was patterned, the supporting tensile SiRN layer ($\sigma_0 = 0.25$ GPa) was replaced by a compressive SiN_x layer ($\sigma_0 = -2$ GPa) (step 5). For this, the SiRN layer is removed using Ar ion beam etch and an 80 nm thick SiN_x layer is then deposited on the bottom side by magnetron sputtering of Si in an $Ar+N_2$ gas mixture. Replacement of the support layer was done in order to prevent uncontrolled continuous crack propagation in the membrane during the following steps of fabrication. A tensile support layer is necessary during the first half of the fabrication process, to allow for the lithography step and prevent buckling and development of stress gradients during $ZrSi_x$ deposition. However, it was observed that the use of the tensile support layer during pattern etching (step 6) almost always resulted in the failure of the whole membrane containing the array of test structures. The reason for this is that if a crack was to originate in one of the test structures, the tensile stress in the partially etched $ZrSi_x$ + SiRN openings (i.e. holes in the test structure pattern) prevented cracks from arresting, allowing them to be transferred from one structure to the next, leading to the failure of the whole membrane. Replacement of the tensile support layer by a compressive one reduced the average stress, preventing such early membrane failure.

After the replacement of the support layer, the test structure pattern was transferred from the Cr layer to the $ZrSi_x$ by an Ar ion beam etch (step 6). The remaining Cr mask was stripped using wet Cr etch, resulting in $ZrSi_x$ layer capped with a 5 nm SiN_x layer from the top side and supported by an 80 nm SiN_x layer on the bottom side (step 7). Following that, an Ar ion beam etch was used to remove the SiN_x layers: first, the top 5 nm cap layer and then the supporting 80 nm layer, resulting in the final released 90 nm thick single layer $ZrSi_x$ crack-on-chip structures (step 8).

To measure the fracture toughness of the $ZrSi_x$ layer, 144 test structures with varied geometries were fabricated, which was done to find the optimal designs that can survive the fabrication without fracturing. More specifically, straight and tapered actuator shapes were used, with the length L_a varied between 60 μm and 120 μm. Furthermore, the width (measured at the narrowest point for the tapered actuators) of the actuators W_a and the sample beam W_s was varied between 10 μm and 30 μm. Despite having more than a hundred samples, only 18 of them survived fabrication. The main reason for this was the use of excessively sharp pre-cracks, which caused a large number of samples to fracture already during fabrication. Since crack propagation, in this case, occurs in the structure with some unknown SiN_x layer remaining, no reliable information on fracture toughness could be extracted for those samples.

V. Fracture Energy Measurements

A. Crack Initiation by FIB

The experimental procedure performed to measure the fracture energy of $ZrSi_x$ thin films consisted of two main steps: 1) triggering crack propagation by FIB and then measuring the lengths of produced cracks, and 2) determining the value of internal stress using the approach described in section III C. These experimental parameters were then used in FEM simulations to calculate values of the G_c for each of the fracture events triggered by FIB. The results of fracture energy measurements are presented and discussed in the next section (section V B), while in this section we describe the details of the FIB procedure.

As mentioned earlier in section II, to initiate fracture in the un-cracked test structures, the blunt pre-cracks produced by photolithography were further "sharpened" using FIB. To do this, a small triangular notch with a length of approximately 1-2 μm and a width of 300-500 nm was milled at tips of the pre-cracks. Milling was done using Ga beam with the beam energy of 30 kV and the current of 26 pA. Depending on the exact size of the milled area, each milling step took approximately 10-30 seconds to complete. It should be mentioned, that damage and ion implantation caused by FIB milling may affect the fracture properties of the material, therefore values of fracture initiation toughness obtained from FIB milled pre-cracks need to be carefully examined in each case [20], [21]. In this study, G_c is evaluated over the whole crack length (in the order of 10 μm), which was significantly larger than the typical size of the FIB damaged area, estimated to be in the order of tens of nanometers [22]. Therefore, the influence of FIB damage on the experimental results is believed to be negligible.

For each sample, FIB milling was done twice, once at each of the two ends of the pre-crack (slit), which resulted in two consecutive fracture events. Lengths of the produced cracks were measured from the FIB images recorder after both first and second fracture, which allowed to extract two fracture energy values per sample.

As noted in section III, quantification of mixed mode rapid crack propagation requires knowledge on the dynamics of crack propagation and movement of the buckled structure, as well a significant modelling effort. Therefore, in this work, focus was made on pure mode I crack propagation and determination of mode I fracture toughness. Among the 18 tested structures, only 10 were successful and resulted in pure mode I fracture. Fig. 7 presents examples of failed and successful samples. Fig. 7a shows an image of a pre-crack with a FIB milled notch, which didn't result in crack initiation due to the insufficient force provided by the actuators used in this particular test sample. Another example of a failure is shown in Fig. 7b. Cracks in this sample deviated from straight trajectory, which then lead to asymmetric (relative to crack propagation direction) buckling. As a result, crack propagated in mixed

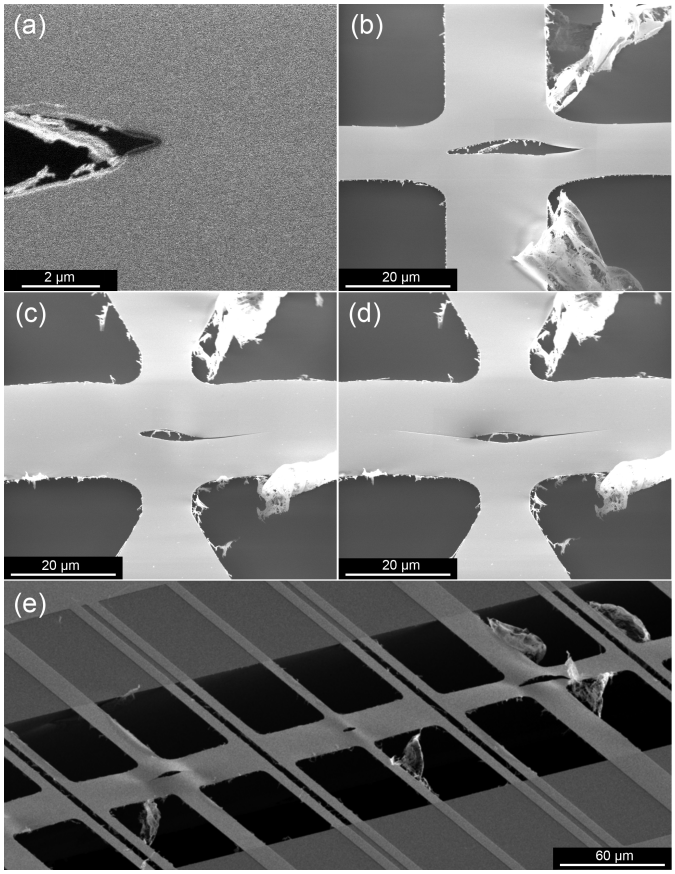

Fig. 7. (a)-(d) FIB images of samples taken during the experiment: (a) pre-crack with a milled notch, which failed to initiate a crack, (b) failed sample with curved crack and asymmetric buckling, leading to mixed mode fracture, (c) and (d) successful sample (#2 in Table I) after first and second fracture, respectively. (e) SEM image taken after the experiment showing entire test structures. The SEM image is taken at large angle to better illustrate the presence of buckling. The debris loosely attached to the edges of the test structure come from the sacrificial SiN_x layer, which could not be fully removed by the directional Ar beam, and can be ignored as they don't exert any force on $ZrSi_x$.

mode conditions, with contributions from all three loading modes being present. It should be noted, that such kinking was always observed, if the initial buckling mode in the un-cracked structure was anti-symmetric (Fig. 3b) or asymmetric (such as Fig. 3d) with respect to the expected crack propagation direction. An example of a successful sample, with both cracks being straight pure mode I cracks, is presented in Fig. 7c-d. In this case (and other successful cases), the buckling profile was symmetric at all times: before the experiment and after first (Fig. 7c) and second (Fig. 7d) fracture events. Image presented in Fig. 7e shows the entire test structures supported by a silicon chip with clearly visible out-of-plane buckling.

One observation made in the experiment, which is important for fracture energy evaluation, is that the length of the crack triggered by the first FIB milling (first crack) in some cases increased upon triggering the second crack by the second FIB milling step. A possible explanation for this effect is the interaction between the tip of the first crack and the stress waves, produced during initiation and propagation of the second crack. Rapid crack propagation, which occurs in cases when the static energy release rate G_s exceeds fracture energy G_c, is known to be accompanied by emission of stress

TABLE I

DIMENSIONS OF THE TEST STRUCTURES AND THE RESULTS OF STRESS AND FRACTURE ENERGY MEASUREMENTS

Actuator shape	#	W_s	W_a	L_a	σ_0	First fracture a_{c1}	First fracture G_c	Second fracture a'_{c1}	Second fracture a_{c2}	Second fracture G_c
		µm	µm	µm	MPa	µm	J/m^2	µm	µm	J/m^2
Tapered at 19°	1	20	10	58.5	489	9.5	22.2±2	9.6	9.8	28.7±3
	2	30	10	66.5	472	14.4	19.9±1.3	15.8	16.4	25.6±2
	3	30	10	63.5	467	8.6	24.1±2	13.7	16.4	21.9±1.7
	4	30	10	61.7	473	8.3	23.2±2	14.6	15.1	21.4±1.6
	Mean				476±9		22.35±2			24.4±3.4
Straight	5	30	20	62.3	470	5.9	32.3±3	7.2	5.9	30±2.5
	6	30	20	65.5	474	10.2	27.2±1.8	10.2	10.6	25.1±1.6
	7	30	20	61.5	484	9.0	26.9±2	9.2	10.7	22.8±1.7
	8	30	20	52.8	471	--		--	7.4	24.3±1.6
	9	30	30	61.5	451	12.3	25±1.3	13.1	12.8	21.6±1.3
	10	30	30	65.5	460	19.9	22.1±1	19.9	16.4	24.3±1.2
	Mean				468±13		26.4±3.2			24.6±2.6
	Total mean				471±11		24.8±3.7			24.6±3

The other relevant structure dimensions, which are not given in the table, were the same between all tested structures: $W_{support} = 10\ um$, $L_s = 60\ um$, $t = 90\ nm$. Note that the presented values of G_c are calculated using the total mean value of internal stress $\sigma_0 = 471 \pm 11\ MPa$, and not the stress values measured for individual samples. The errors given for individual G_c values were determined from the uncertainties in geometric parameters (estimated to be 0.5 um for crack lengths and L_a, and 0.2 um for the other parameters) and the 2.3% standard deviation of internal stress values from the mean (which by itself resulted in 4.6% error in G_c). Errors given for mean values represent standard deviation from the mean.

waves, which propagate and reflect within the material [23]. Interaction of the stress waves with the crack affects the stress distribution at the crack tip, and, as a result, can influence crack propagation behaviour [23], [24]. We suspect, that the increase of stress intensity at the tip of the first crack caused by the arrival of stress waves generated by the initiation (and further propagation) of the second crack is the most likely reason for elongation of the first crack during the second fracture event. Along with propagation of the second crack, this additional elongation of the first crack is responsible for dissipation of the elastic energy released during second fracture and has to be considered in the fracture energy evaluation. Calculation of the fracture energy for the second fracture event was done using the following expression, which takes elongation of the first crack into account:

$$G_c = \frac{1}{t}\frac{U\left(a_{c1},0\right) - U\left(a'_{c1},a_{c2}\right)}{a_{c2} + \left(a'_{c1} - a_{c1}\right)} \tag{5}$$

where t is the thickness of the film, a_{c1} and a'_{c1} are the values of the first crack length measured before and after second fracture event, a_{c2} is the length of the second crack, $U\left(a_{c1},0\right)$ and $U\left(a'_{c1},a_{c2}\right)$ are the values of elastic energy stored in the thin film structure before and after second fracture obtained by FEM. For the first fracture event, fracture energy was calculated using the following expression:

$$G_c = \frac{1}{t}\frac{U\left(0,0\right) - U\left(a_{c1},0\right)}{a_{c1}} \tag{6}$$

where $U\left(0,0\right)$ is the elastic energy before the first fracture.

B. Internal Stress Measurements

Apart from the lengths of produced cracks, evaluation of fracture energy requires knowledge of the elastic properties of the thin film, such as Young's modulus E, Poisson ratio υ an internal stress σ_0. Young's modulus of $ZrSi_x$ was measured

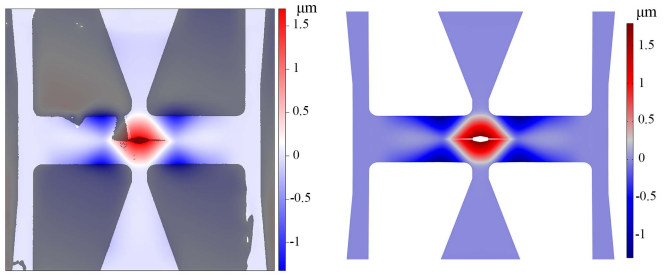

(a) Experimental (b) FEM

Fig. 8. Experimentally measured (a) and simulated (b) out-of-plane displacement distributions (corresponding to sample #2 in Table 1). The "gaps" in the experimental height profile are an artifact of measurement, caused by the insufficient resolution of the camera used to record the interference fringes. Thin film parameters used in the simulation: =180GPa, $\upsilon = 0.2$, $t = 90$nm. For the presented sample, value of internal stress $\sigma_0 = 472$MPa was obtained by fitting the magnitude of the simulated buckling profile to the experimentally measured one.

in a separate experiment using bulge text method. Assuming the value of Poisson ratio $\upsilon = 0.2$ [25], the value of Young's modulus was determined to be $E = 180$GPa. Internal stress σ_0 was determined for individual samples from the magnitude of buckles, which, as discussed in section III C, is uniquely defined by the $\frac{\sigma_0(1-\upsilon)}{E}$ ratio. To do this, for each of the fractured samples, buckling profile measurement was done using white light interferometer (WLI), example of which is given in Figure 8a. After that, series of FEM simulations (example of one such simulation is given in Fig. 8b) were performed to fit the results of WLI measurements and determine σ_0. After the first simulation, which was done using guessed value of σ_0, the obtained out-of-plane displacement distribution was scaled to fit the experimental profile (by minimizing the root mean square difference between the overlapped simulated and measured profiles) and obtain a more accurate estimation of σ_0 in the real structures. The second FEM simulation was then performed using the refined value of σ_0 and the procedure was repeated again. Typically, after third or fourth simulation, further iterations did not lead to any significant (<1%) change in the fitted internal stress value.

The internal stress values obtained this way for each sample are given in Table 1 (along with the results of fracture energy measurements, which are discussed in the next section). From the measured values, the average internal stress in $ZrSi_x$ layer was determined to be $\sigma_0 = 471 \pm 11GPa$. The results of stress measurements show relatively small standard deviation of 2.3%, while maximum and minimum values deviate from the average by about 4%. We believe, that this variance was primarily caused by the methodology, rather than the actual differences of the internal stress in different samples. While the overall shape of the buckling profile obtained in simulations always matched the experimentally measured one, minor differences between the two profiles still could be found upon closer inspection. For example, it was observed, that the exact shape and amplitude of formed buckles was sensitive to the shape and dimensions of the central pre-crack slit, which was found to be slightly different between the individual samples (presumably because of uneven contact between the mask and the membranes during lithography) and was not matched perfectly in the simulations.

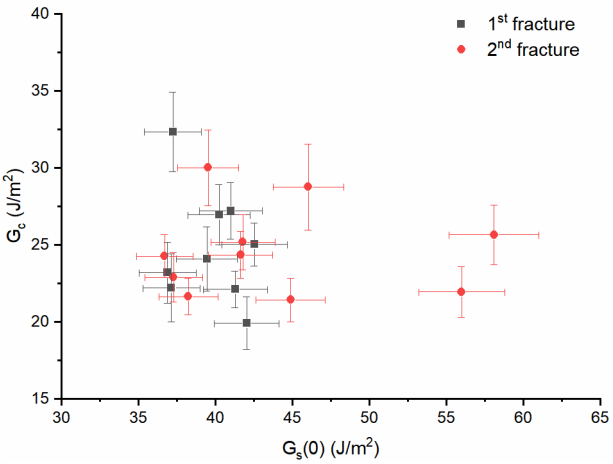

Fig. 9. Fracture energies G_c plotted against the initial static energy release rate at the start of the crack propagation $G_s(0)$.

C. Results and Discussion

For the 10 successful samples, which showed pure mode I fracture, fracture energies were calculated. The dimensions of the test structures and cracks used in the calculations are given in Table I. Note that G_c calculation for each sample was performed using the average internal stress $\sigma_0 = 471 \pm 11GPa$, and not the individual values measured for each sample, since it is believed that the variance in the measured values is primarily caused by the used methodology and not the actual difference in stress between the samples. In 9 samples cracks were successfully initiated on both ends of the slit, allowing to extract two fracture energy values, one for each fracture event, while in one of the samples (#8) only one crack could be initiated. The extracted values of G_c, given in Table I, range between 19.9 and 32.3 J/m^2 with the total average of 24.7±3 J/m^2 and show no significant variation between first and second fracture events or between different actuator designs used. This value of fracture energy corresponds to a mode I fracture toughness of $K_{IC} = 2.1 \pm 0.13$MPa$*$m$^{0.5}$, which is, to the best of our knowledge, the first reported fracture toughness value for $ZrSi_x$ thin films and Zr-Si compounds in general. The obtained fracture toughness is typical for a brittle material and is similar to the fracture toughness measured for some other transition metal silicides, such as $NbSi_2$ (1.5-2 MPa*m$^{0.5}$ for the single crystal [26]) and $MoSi_2$ (1.5-5 MPa*m$^{0.5}$ for sintered and thermally sprayed $MoSi_2$ polycrystals [27]–[29]). However, it should be noted, that direct comparison with the available literature data has limited value due to the differences in the measurement methods.

It is known that crack velocity can influence fracture toughness [30]–[33]. Therefore, it is important to discuss the relation of the G_c values obtained from rapid crack propagation to fracture energy of slow stable crack propagation. In brittle materials, the velocity toughening effect (the increase of fracture energy/fracture toughness with the increase of crack velocity) has been attributed to enhanced thermal phonon emission, an increase of fracture surface roughness, and crack branching [30]–[32]. In turn, the crack velocity itself is dependent on the elastic energy release rate G_s, which drives

the crack propagation. Previously, it was shown [33], that in DCB structures, similar to the structures used in this work, cracks propagate with a near-constant velocity determined by the value of the elastic energy release rate at the start of propagation $G_s(0)$. Hence, it is expected, that cracks characterized by higher values of $G_s(0)$ (initial energy release rate, i.e. at zero crack length) should also exhibit higher fracture energy G_c. To see, whether this effect takes place in this experiment, G_c was plotted against the initial energy release rate $G_s(0)$, which is also the highest value of G_s during the whole crack propagation. The data, presented in Fig. 9, suggests that there exist no significant correlation between the initial energy release rate $G_s(0)$ and fracture energy G_c. The variation in the G_c values, instead, can be explained by the experimental errors and local variations in fracture toughness arising from the microstructure. However, due to the large spread and uncertainty in the measured G_c values, as well relatively small range of covered $G_s(0)$ values, the observed absence of correlation between G_c and $G_s(0)$ does not confirm that velocity toughening effect did not take place in the experiment. Given the scarcity of studies in the area of free-standing thin film fracture, the influence of crack velocity on fracture energy needs further investigation. In particular, a direct comparison between the fracture energy values measured for rapid and slow fracture regimes would be of most interest. Such studies would allow to get a better understanding of the energy dissipation mechanisms and prevent apparent inconsistencies between the fracture toughness results obtained by different methods. This, however, will require further development of fracture toughness measurement techniques for free-standing thin films, which are still underdeveloped in comparison with the techniques available for bulk and micron-sized materials. For example, adding a possibility to apply controlled mechanical load to the crack-on-a-chip test structures, would allow for direct comparison between rapid and slow fracture regimes, whereas crack velocity measurements and dynamic mechanical analysis [34], should make it possible to quantify the velocity toughening effect.

VI. Conclusion

In this work, the crack-on-a-chip test method was used to study the fracture of free-standing $ZrSi_x$ thin films. Rapid crack propagation, initiated by FIB milling in vacuum to avoid environmental effect on fracture process, followed by crack arrest was used to obtain the mode I fracture toughness values. FEM simulations showed that out-of-plane deformations observed in the thin film structures are caused by the buckling instability and have a strong effect on the energy release rates, driving crack propagation. To produce free-standing $ZrSi_x$ thin film structures, a generic fabrication process was developed, which can be universally applied for other thin film materials without concerns for chemical etch selectivity due to the use of physical etching for the thin film structure release. We report, for the first time, a fracture toughness value for $ZrSi_x$ of $K_{IC} = 2.1 \pm 0.13$ MPa $*$ m$^{0.5}$.

References

[1] G. A. Papadopoulos and P. I. Poniridis, "Crack initiation under biaxial loading with higher-order approximation," *Eng. Fract. Mech.*, vol. 32, no. 3, pp. 351–360, Jan. 1989.

[2] V. N. Shlyannikov and A. V. Tumanov, "An inclined surface crack subject to biaxial loading," *Int. J. Solids Struct.*, vol. 48, nos. 11–12, pp. 1778–1790, Jun. 2011.

[3] P. J. van Zwol *et al.*, "Pellicle films supporting the ramp to HVM with EUV," *Proc. SPIE*, vol. 10451, Oct. 2017, Art. no. 104510O.

[4] J. A. Liddle, H. A. Huggins, P. Mulgrew, L. R. Harriott, H. H. Wade, and K. Bolan, "Fracture strength of thin ceramic membranes," *MRS Proc.*, vol. 338, no. 1, pp. 501–506, 1994.

[5] B. Merle and M. Göken, "Fracture toughness of silicon nitride thin films of different thicknesses as measured by bulge tests," *Acta Mater.*, vol. 59, no. 4, pp. 1772–1779, Feb. 2011.

[6] H. Kahn, N. Tayebi, R. Ballarini, R. L. Mullen, and A. H. Heuer, "Fracture toughness of polysilicon MEMS devices," *Sens. Actuators A, Phys.*, vol. 82, nos. 1–3, pp. 274–280, May 2000.

[7] J. J. Bellante, H. Kahn, R. Ballarini, C. A. Zorman, M. Mehregany, and A. H. Heuer, "Fracture toughness of polycrystalline silicon carbide thin films," *Appl. Phys. Lett.*, vol. 86, no. 7, pp. 1–3, 2005.

[8] H. D. Espinosa and B. Peng, "A new methodology to investigate fracture toughness of freestanding MEMS and advanced materials in thin film form," *J. Microelectromech. Syst.*, vol. 14, no. 1, pp. 153–159, 2005.

[9] I. Chasiotis, S. W. Cho, and K. Jonnalagadda, "Fracture toughness and subcritical crack growth in polycrystalline silicon," *J. Appl. Mech.*, vol. 73, no. 5, p. 714, Sep. 2006.

[10] S. Jaddi, M. Coulombier, J.-P. Raskin, and T. Pardoen, "Crack on a chip test method for thin freestanding films," *J. Mech. Phys. Solids*, vol. 123, pp. 267–291, Feb. 2019.

[11] W. Broughton, "Testing the mechanical, thermal and chemical properties of adhesives for marine environments," in *Adhesives in Marine Engineering*. Sawston, U.K.: Woodhead Publishing, 2012, pp. 99–154.

[12] S. Jaddi, J.-P. Raskin, and T. Pardoen, "On-chip environmentally assisted cracking in thin freestanding SiO_2 films," *J. Mater. Res.*, vol. 36, no. 12, pp. 1–16, 2021.

[13] B. Lawn, "Unstable crack propagation: Dynamic fracture," in *Fracture of Brittle Solids*. Cambridge, U.K.: Cambridge Univ. Press, 2010, pp. 86–105.

[14] M. D. Thouless and R. F. Cook, "Stress-corrosion cracking in silicon," *Appl. Phys. Lett.*, vol. 56, no. 20, pp. 1962–1964, 1990.

[15] S. M. Barinov, L. V. Fateeva, V. J. Shevchenko, B. Ballokova, P. Hvizdoš, and E. Rudnayová, "Stress-corrosion cracking in alumina ceramics," *Key Eng. Mater.*, vol. 223, pp. 187–192, Feb. 2002.

[16] COMSOL. (2020). *COMSOL Multiphysics Documentation*. [Online]. Available: http://www.comsol.com

[17] F. G. Rammerstorfer, "Buckling of elastic structures under tensile loads," *Acta Mech.*, vol. 229, no. 2, pp. 881–900, Feb. 2018.

[18] A. Shafikov *et al.*, "Strengthening ultrathin Si_3N_4 membranes by compressive surface stress," *Sens. Actuators A, Phys.*, vol. 317, Jan. 2021, Art. no. 112456.

[19] M. Croisy *et al.*, "Characterization of photoresist films exposed to high-dose implantation conditions," *J. Vac. Sci. Technol. B, Nanotechnol. Microelectron., Mater., Process., Meas., Phenomena*, vol. 36, no. 1, Jan. 2018, Art. no. 011201.

[20] E. I. Preiß *et al.*, "Applicability of focused ion beam (FIB) milling with gallium, neon, and xenon to the fracture toughness characterization of gold thin films," *J. Mater. Res.*, vol. 36, no. 12, pp. 2505–2514, Jun. 2021.

[21] S. Ogihara, Y. Imafuku, R. Yamamoto, and Y. Kogo, "Application of FIB technique to introduction of a notch into a carbon fiber for direct measurement of fracture toughness," *J. Phys., Conf. Ser.*, vol. 191, Nov. 2009, Art. no. 012009.

[22] E. Preiß, "Fracture toughness of freestanding metallic thin films studied by bulge testing," Ph.D. dissertation, Fac. Eng., FAU, Nuremberg, Germany, 2018.

[23] D. Massy *et al.*, "Crack front interaction with self-emitted acoustic waves," *Phys. Rev. Lett.*, vol. 121, no. 19, Nov. 2018, Art. no. 195501.

[24] K. Ravi-Chandar and W. G. Knauss, "An experimental investigation into dynamic fracture: IV. On the interaction of stress waves with propagating cracks," *Int. J. Fract.*, vol. 26, no. 3, pp. 189–200, Nov. 1984.

[25] S. Shu, F. Guo, and Y. Zhan, "*Ab initio* insight into the structure and properties of Zr–Si system," *Phys. Status Solidi Basic Res.*, vol. 256, no. 10, pp. 1–8, 2019.

[26] K. Hagihara and T. Nakano, "Fracture behavior and toughness of $NbSi_2$-based single crystals and $MoSi_2(C11_b)$/$NbSi_2(C40)$ duplex crystals with a single set of lamellae," *Acta Mater.*, vol. 59, no. 10, pp. 4168–4176, Jun. 2011.

[27] D. G. Morris, M. Leboeuf, and M. A. Morris, "Hardness and toughness of $MoSi_2$ and $MoSi_2$–SiC composite prepared by reactive sintering of powders," *Mater. Sci. Eng. A*, vol. 251, nos. 1–2, pp. 262–268, Aug. 1998.
[28] A. C. E. Silva and M. J. Kaufman, "Applications of *in situ* reactions to $MoSi_2$-based materials," *Mater. Sci. Eng. A*, vol. 195, pp. 75–88, Jun. 1995.
[29] J. Sun, Q.-G. Fu, C.-X. Huo, and T. Li, "Fracture toughness of thermally sprayed $MoSi_2$ composite with different melting indices," *Compos. B, Eng.*, vol. 150, pp. 242–247, Oct. 2018.
[30] D. Sherman, "Aspects of rapid crack propagation in silicon," *Fatigue Fract. Eng. Mater. Struct.*, vol. 30, no. 1, pp. 32–40, Jan. 2007.
[31] S. Salih, K. Davey, and Z. Zou, "Rate-dependent elastic and elasto-plastic cohesive zone models for dynamic crack propagation," *Int. J. Solids Struct.*, vol. 90, pp. 95–115, Jul. 2016.
[32] J. Swadener, M. Baskes, and M. Nastasi, "Molecular dynamics simulation of brittle fracture in silicon," *Phys. Rev. Lett.*, vol. 89, no. 8, pp. 19–22, Aug. 2002.
[33] M. F. Kanninen, "A dynamic analysis of unstable crack propagation and arrest in the DCB test specimen," *Int. J. Fract.*, vol. 10, no. 3, pp. 415–430, Sep. 1974.
[34] T. Cramer, A. Wanner, and P. Gumbsch, "Energy dissipation and path instabilities in dynamic fracture of silicon single crystals," *Phys. Rev. Lett.*, vol. 85, no. 4, pp. 788–791, Jul. 2000.

Airat Shafikov received the B.Sc. and M.Sc. (Hons.) degrees from the Moscow Institute of Physics and Technology in 2015 and 2017, respectively. He is currently pursuing the Ph.D. degree with the Industrial Focus Group XUV Optics, Mesa+ Institute, University of Twente. His research interests include synthesis and study of mechanical properties of nanoscale-thin freestanding films.

Robbert van de Kruijs has been involved in the development of thin film coatings for mainly x-ray and neutron applications for over 20 years. His field of interest ranges from fundamental layer growth and atomic scale interactions towards application relevant topics, such as thermal damage, optics contamination, and spectral filtering. He is currently involved in various EUVL related research and development projects within the XUV Focus Group, MESA+ Institute, University of Twente, exploring industrially relevant topics, such as optics lifetime, protective pellicles, and advanced reticle architectures.

Jos Benschop received the M.Sc. *(cum laude)* and Ph.D. degrees from the Physics Faculty, Twente University. From 1984 to 1997, he worked at Philips on optical metrology and optical recording. He joined ASML in 1997. As a Senior Vice President Technology, he is currently responsible for research and system engineering within ASML. He is an SPIE Fellow and a part-time Professor at the NNV leerstoel Industriële Natuurkunde, University of Twente. He has published more than 30 papers and generated more than 20 patents. He is a member of the Netherlands Academy of Technology and Innovation (https://www.acti-nl.org/nl). He has been appointed by the Dutch King as an Advisor to the Dutch Government on Science, Technology and Innovation (https://www.awti.nl/).

Wesley van den Beld received the Ph.D. degree (Hons.) in electrical engineering from the BIOS Lab-on-Chip Group, with a focus on graphene and permalloy integration in functional fluidic and solid-state devices, exploiting advanced clean room technologies. Then, he has been engaged in the synthesis of nanoscale-thin pellicles for mask application in the XUV group. He also avails of a relevant set of contacts at ASML and elsewhere and is currently well embedded in the MESA+ NanoLab community.

Silvester Houweling received the M.Sc. degree in physics from Universiteit Utrecht in 2007, with a focus on silicon nitride thin films for photovoltaics and thin film transistors, and the Ph.D. degree in experimental physics from Universiteit Utrecht in 2011, with a focus on syntheses and characterizations of nanostructured films, such as carbon nanotubes for photovoltaics and tungsten oxide nanostructured films for smart windows. Since 2012, he has been working as a Senior Research Scientist at ASML, predominantly on the development of EUV pellicles. He is currently a Visiting Fellow at the XUV Focus Group, University of Twente. He has published 37 papers and has generated seven patents related to EUV pellicles. He is active for the European Commission as a Project Monitor and a Proposal Evaluator (Horizon 2020).

Fred Bijkerk received the Ph.D. degree in experimental physics from the University of Amsterdam in 1993. From 2004 to 2014, he was the Department Head of the FOM-Institute for Plasma Physics Rijnhuizen. In 2005, he was appointed as a Professor on XUV sources and multilayer optics at the MESA+ Institute for Nanotechnology, University of Twente. He initiated the Industrial Focus Group XUV Optics, MESA+, a public-privately funded research initiative on application-inspired thin film systems and XUV optics. He received the FOM Valorization Prize in 2011. He has published over 250 journal articles and 35 patents on thin film systems and XUV optics.